Lattice dynamics of the polar orthorhombic phase of HfO_2

Shiyu Fan,[1,2] Sobhit Singh,[1,3] Xianghan Xu,[3,4] Kiman Park,[5] Yubo Qi,[3] S. W. Cheong,[3,4] David Vanderbilt,[3] Karin M. Rabe,[3] and J. L. Musfeldt[5,2]

[1]*These authors contributed equally to this work*

[2]*Department of Physics and Astronomy,*
University of Tennessee, Knoxville, Tennessee, 37996, USA

[3]*Department of Physics and Astronomy,*
Rutgers University, Piscataway, New Jersey 08854, USA

[4]*Rutgers Center for Emergent Materials,*
Rutgers University, Piscataway, New Jersey 08854, USA

[5]*Department of Chemistry, University of Tennessee, Knoxville, Tennessee, 37996, USA*

(Dated: October 11, 2021)

Abstract

Hafnia (HfO_2) is a promising material for emerging chip applications due to its high-κ dielectric behaviour, suitability for negative capacitance heterostructures, and scalable ferroelectricity together with silicon technology compatibility. The lattice dynamics along with phononic properties such as thermal conductivity and contraction as well as heat capacity are under-explored, primarily due to the absence of high quality single crystal specimens. Herein, we report the vibrational properties of a series of HfO_2 crystals stabilized with yttrium (chemical formula HfO_2:xY, where x = 20, 12, 11, 8, and 0%) and compare our findings with a symmetry analysis and lattice dynamics calculations. We test our calculated spectra against the measured Raman and infrared reflectance response of the cubic, antipolar orthorhombic, and monoclinic phases in order to disentangle the impact of Y incorporation. This includes a resonance background in the Raman scattering spectrum, a weak metallic response in the infrared reflectance, and local symmetry breaking which activates otherwise silent vibrational features. With these issues on a firm foundation, we address the lattice dynamics of the polar orthorhombic phase of HfO_2:12%Y. Here, we uncover a number of signature modes involving polar displacements as well as Hf–Hf dimer breathing modes that are connected with ferroelectric polarization in orthorhombic polar hafnia. This work provides a spectroscopic fingerprint for several different phases of HfO_2 and, at the same time, paves the way for a detailed analysis of mode contributions to the high-κ dielectric and ferroelectric properties that are at the heart of emerging chip technologies.

INTRODUCTION

Phonons in HfO_2 are key to understanding competing phases and physical properties of this emerging scientifically and technologically important material, unlocking the door to discoveries in fields as diverse as thin film dielectrics and nanoscale devices and photonics.[1–18] It has recently been discovered that flat phonon bands have a direct connection to the unique energy landscape in the vicinity of the ferroelectric phase.[12] This originates from the alternatively ordered spacer and polar HfO_2 layers, which creates very localized electric dipoles within the irreducible half-unit cell widths (≈3 Å) of HfO_2.[12] The nanometer-scale dipoles are individually switchable without any net energy cost, though with energy barriers that correspond to very large coercive fields.[6–8] Physical properties determined by phonons include heat capacity and thermal conductivity behavior, with heat management in memory and logic devices being vital for technological applications.

HfO_2 is highly polymorphic, with many competing phases generated by different distortions of the high-symmetry cubic fluorite structure.[11,13–17,19–23] The cubic (c) $Fm\bar{3}m$ fluorite phase itself is stabilized only at very high temperatures (> 2900 K).[5,17,24] Upon cooling, this phase transforms to a lower symmetry tetragonal (t) $P4_2/nmc$ phase in temperature range 2900 – 2073 K. At room temperature, hafnia stabilizes in a monoclinic (m) $P2_1/c$ phase, which is the ground state phase of bulk hafnia at ambient conditions. Furthermore, two orthorhombic metastable polar (*o-III*) $Pca2_1$ and antipolar (*o-AP*) $Pbca$ phases of hafnia are reported at higher pressures.[15–17,25–27] Figure 1 summarizes the crystal structures of these five different phases along with their calculated phonon dispersions, showing that all except the cubic phase are locally stable. The cubic-tetragonal phase transition is driven by an unstable zone-boundary X_2^- phonon mode of the c phase. Ferroelectricity in the polar o-III phase of hafnia can be understood in reference to a high-symmetry centrosymmetric tetragonal phase. Remarkably, there is no unstable polar mode in the high-symmetry tetragonal reference structure. Rather, first principles calculations have shown that the key factor in stabilizing the orthorhombic polar phase is a strong trilinear coupling among polar, nonpolar, and antipolar phonon modes.[23,28] We note that the presence of oxygen vacancies, doping, substrate-induced strain, and disorder have been reported to stabilize various other phases of hafnia,[9,11,14,19–21,29–32] which are not within the scope of the present investigation.

For almost a decade, the observation of ferroelectricity in hafnia has been limited only to thin films.[4–6,9,29–34] Stabilization of the orthorhombic polar phase in bulk form is not trivial.[13,14] This is because the orthorhombic polar phase is predicted to be metastable, and it requires very high temperatures to form.[17] There have been a number of attempts to prepare the elusive ferroelectric phases of hafnia at ambient conditions. Ultra-thin films HfO_2:Si have been synthesized to obtain the ferroelectric phases,[4–7,10,29–31,33,34] although it is challenging to characterize these phases due to their small domain size and substrate effects. A rhombohedral ferroelectric phase was recently reported in epitaxially strained $Hf_{0.5}Zr_{0.5}O_2$ thin

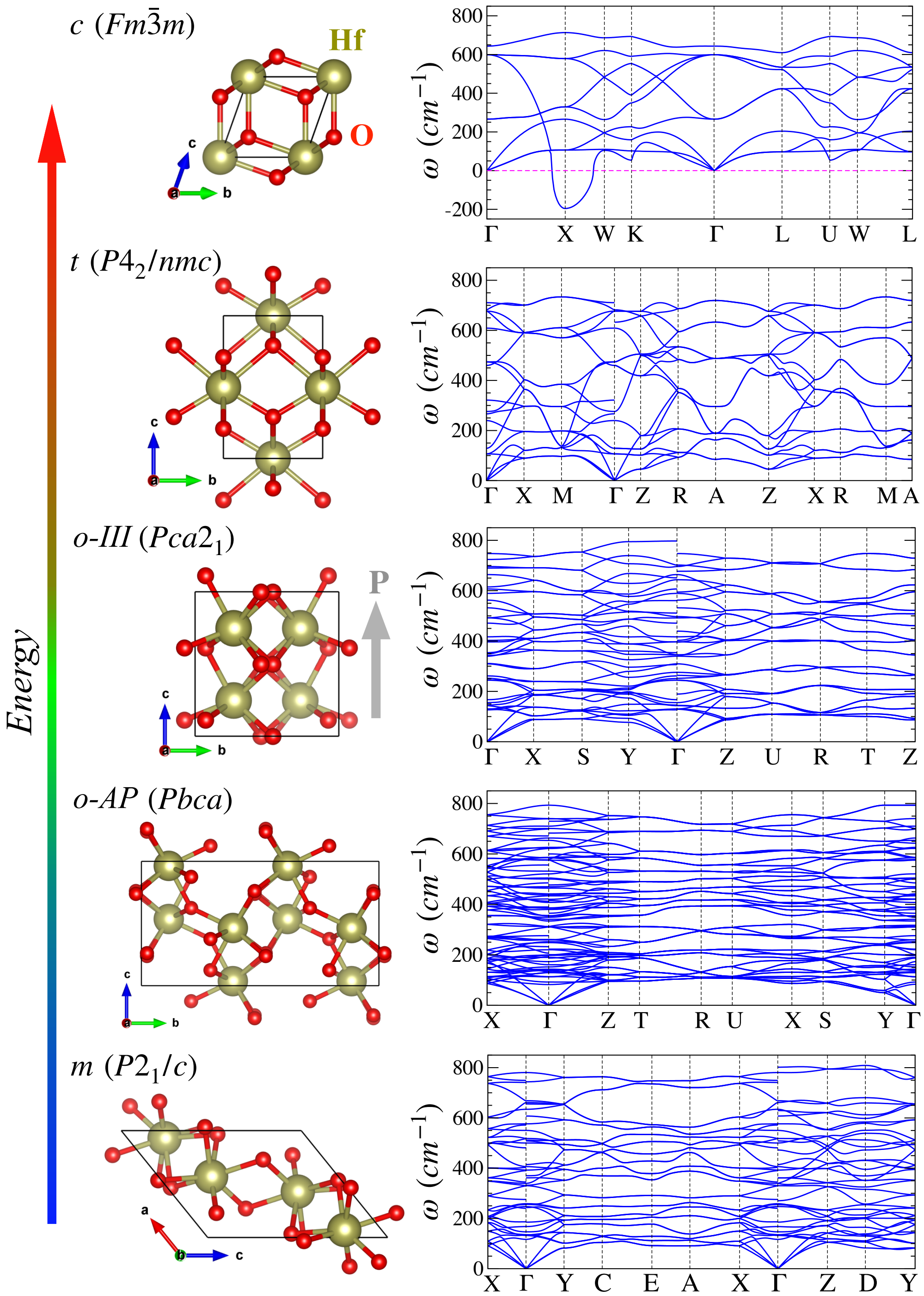

Figure 1. Crystal structure and calculated phonon dispersions of the five studied phases of bulk HfO$_2$. These include: cubic (*c*), tetragonal (*t*), orthorhombic polar (*o-III*), orthorhombic antipolar (*o-AP*), and monoclinic (*m*), arranged in the order of their increasing formation energy. The *c* phase has the highest formation energy, whereas the *m* phase has the lowest formation energy. The gray arrow denotes the direction of the ferroelectric polarization (**P**) in the *o-III* phase.

films also illustrating the complex interplay between the film and substrate.[9,30] First principles calculations show that distinct competing ferroelectric phases can be stabilized in hafnia via epitaxial strain.[20] Ferroelectricity in hafnia depends intimately on the concentration of oxygen vacancies as well.[32,35]

Recently, Xu *et al.* demonstrated the stabilization of the polar *o-III* phase of hafnia as well as the antipolar *o-AP* phase in bulk single crystals grown using laser-diode-heated floating zone techniques.[13] Yttrium substitution and a rapid cooling rate are key to realizing the polar *o-III* and antipolar *o-AP* phases at ambient conditions.[13] Ferroelectricity in the *o-III* phase was experimentally demonstrated with a switchable polarization and a magnitude $3\,\mu\mathrm{C/cm}^2$ together with a coercive electric field of $4\,\mathrm{MV/cm}$.[13] The availability of high-quality single crystals creates a number of exciting opportunities to examine the properties of this family of materials - especially those of the more elusive members. While phonons in the cubic, tetragonal, and monoclinic phases have been investigated in prior work,[16,22,25,26,36–44] the lattice dynamics of the orthorhombic polar and antipolar phases are wholly unexplored. In addition to providing a spectroscopic fingerprint for the different phases of HfO_2, this work opens the possibility of analyzing structure-property trends in the phonon excitation spectrum and Born effective charges, as in a recent work on the heavy chalcogenide 1T-HfS_2 in which it was found that the enhanced Born charge of hafnium is attributable to polar displacement-induced charge transfer from sulfur to hafnium.[45]

In this work, we build upon these recent advances by measuring the infrared- and Raman-active phonons in the two orthorhombic phases of hafnia. We compare our results with the spectroscopic response of the cubic and monoclinic phases as well as a symmetry analysis and complementary lattice dynamics calculations, including analysis of the anomalous Born effective charges. Taken together, our work places the vibrational properties of HfO_2 on a secure footing and paves the way for an advanced understanding of properties that depend upon the fundamental excitations of the lattice.

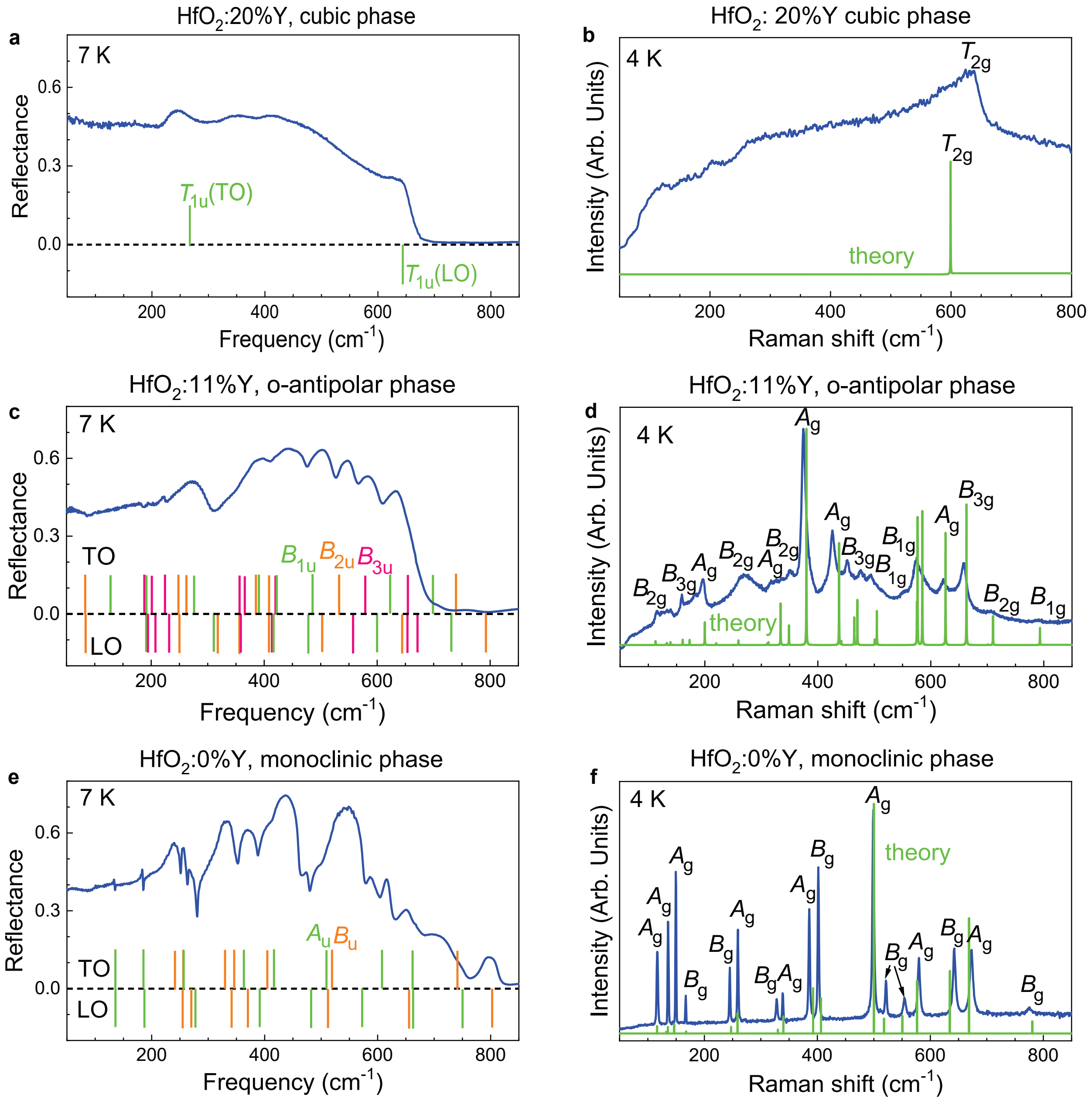

Figure 2. **a,** Infrared reflectance spectrum of the cubic HfO_2:20%Y at 7 K. **b,** Raman spectrum of the cubic HfO_2:20%Y at 4 K. **c,** Infrared reflectance spectrum of the o-AP HfO_2:11%Y at 7 K. **d,** Raman spectrum of the o-AP HfO_2:11%Y at 4 K. **e,** Infrared reflectance spectrum of the monoclinic HfO_2 at 7 K. **f,** Raman spectrum of the monoclinic HfO_2 at 4 K. The theoretical peak positions of the infrared TO and LO modes in pure HfO_2 are marked using vertical upward and downward lines, respectively (details in the Supporting Information). The calculated Raman spectrum of pure HfO_2 (arb. units) is plotted along with the measured Raman spectrum using green lines.

RESULTS AND DISCUSSION

Understanding the spectroscopic properties of cubic HfO_2:20%Y

In order to investigate the lattice dynamics in different phases of hafnia, we systematically performed infrared reflectance and Raman-scattering measurements in near normal incidence and back-scattering geometry, respectively, using unpolarized light. Figure 2a,b displays the infrared reflectance and Raman scattering response of cubic HfO_2:20%Y. Only two triply-degenerate vibrational modes are predicted at zone center in the pure cubic HfO_2 phase. The T_{1u} mode at 266 cm^{-1} and T_{2g} mode at 599 cm^{-1} are infrared- and Raman-active, respectively [Table S5, Supporting Information]. However, they can both be active in the experimental infrared and Raman spectra because of local symmetry-breaking induced by yttrium incorporation [Fig. S1c, Supporting Information]. The T_{1u} mode splits into longitudinal optic (LO) and two transverse optic (TO) modes near the zone center at nonzero wavevector ($\mathbf{q} \to \mathbf{0}$). The calculated frequency of the T_{1u}(LO) mode is 643 cm^{-1}. In our measured infrared reflectance spectrum, we clearly observe the signatures of the T_{1u}(TO) and T_{1u}(LO) modes, even though the T_{1u}(LO) mode overlaps with the nearby T_{2g} mode. The overlap between the two modes broadens the observed feature around 620 cm^{-1} in the infrared reflectance spectrum. The T_{2g} mode is also clearly detected in the measured Raman response.

The overall agreement between our measurements and the predicted phonon frequencies is reasonable. But more than a simple match, these data reveal the challenges with Y incorporation - even in this straightforward cubic system. The Raman scattering spectrum, for instance, has a noticeable fluorescence background that varies with excitation laser wavelength, and the scattering intensity depends upon the measurement spot due to surface roughness and cracking. At the same time, a weak metallic response develops in the reflectance spectrum due to the Y inclusion. This type of weak metallicity is seen in other materials including Y-stabilized zirconia (ZrO_2:Y_2O_3) due to oxygen deficiencies[46–48] as well as Nb-substituted $EuTiO_3$ and Pb-substituted $BaPb_xBi_{1-x}O_3$ due to added carriers.[49–51] In any case, in our results, the over-damped Drude[50] partially screens the T_{1u} phonon. At the same time, Y incorporation breaks local symmetry and activates several additional vibrational modes arising from Y sublattice. This is apparent in both the infrared and Raman response and occurs primarily below 400 cm^{-1}. This is consistent with our calculations for the ground state configuration of Y-substituted cubic HfO_2 [Fig. S1, Supporting Information]. Fortunately, weak metallicity and the presence of a few additional vibrational features do not interfere with identifying the fundamental T_{1u} and T_{2g} vibrational modes in cubic HfO_2:20%Y. These effects are diminished (but not absent) in the orthorhombic materials discussed below because the overall level of Y incorporation is significantly lower and therefore much less important.

Testing our predictions on antipolar orthorhombic HfO_2:11%Y

Figure 2c displays the infrared spectrum of HfO_2 with 11% Y substitution. This material is orthorhombic and antipolar (*Pbca*, *o-AP*). The weak metallic background in the infrared reflectance is overall reduced compared to that in HfO_2:20%Y sample, and phonon screening is considerably weaker. As a result, all of the infrared-active phonons are sharper and better resolved. This effect is even more obvious in the 8% sample [Fig. S4, Supporting Information], where the orthorhombic and monoclinic phases are mixed. The comparison between experiment and theory is good overall, even though the infrared-active phonons are partially screened by the weak metallic background induced by Y incorporation. Fortunately, the Raman-active phonons are well-resolved, providing an even better opportunity to compare experiment and theory. Figure 2d displays the Raman scattering spectrum of HfO_2:11%Y. Numerous Raman-active peaks are present due to the lower crystal symmetry compared to the cubic case, and the fluorescence background has been dramatically reduced using a longer wavelength laser ($\lambda = 532$ nm). Compared to HfO_2:20%Y, there are fewer phonon modes activated due to Y incorporation and the subsequent symmetry breaking. Overall, our experimental results nicely match the theoretical predictions in terms of both frequency and intensity.

Lattice dynamics of the monoclinic phase of HfO_2:0%Y

The monoclinic phase is the ground state of bulk hafnia, so it is easy to stabilize this phase in single-crystal form without any Y substitution. Figure 2e,f summarizes the infrared reflectance and Raman scattering response of this phase. Since there is no Y incorporation, the infrared-active phonons are well defined and unscreened, and the fluorescence background observed in the samples containing 20 and 11% Y is absent. The overall agreement between the measured and calculated pattern of excitations for pure hafnia is excellent and in perfect agreement with prior literature.[40,42,43] This illustrates the predictive power of theory and quality of vibrational spectra that should be available once the need for Y inclusion in the crystal growth process is eliminated.

Revealing the vibrational properties of orthorhombic polar HfO_2:12%Y

After developing an in-depth understanding of the lattice dynamics and vibrational signatures of the above-studied phases of hafnia, we turn our attention to the polar orthorhombic (*o-III*) phase, which is central to this study. Figure 1 displays the crystal structure of the *o-III* phase, which was experimentally stabilized by 12% Y substitution on the Hf lattice at rapid cooling conditions.[13] A complex trilinear coupling involving a zone-center polar (Γ_3^-), and zone-boundary nonpolar (Y_2^+) and antipolar (Y_4^-) phonon modes is responsible for the ferroelectric polarization in the *o-III* phase.[23,28] More simplistically, one can attribute ferroelectricity in this phase to the polar distortion of oxygen atoms along the $\vec{c}$ axis (in reference to a centrosymmetric tetragonal phase) as shown in Fig. 3(e), resulting in a spontaneous ferroelectric polarization ($\boldsymbol{P}$) parallel to the $\vec{c}$ lattice vector (or $\hat{z}$ direction).[12,23]

The primitive unit cell of *o-III* phase contains a total of 12 atoms (4 formula units) resulting in 33 optical phonon modes having following irreducible representations at the zone center:

$$\Gamma_{o\text{-}III} = 8\,A_1 \oplus 9\,A_2 \oplus 8\,B_1 \oplus 8\,B_2. \tag{1}$$

The A_1, B_1, and B_2 modes are infrared active, generating changes in the dipole moment along the $\hat{z}$, $\hat{x}$, and $\hat{y}$ directions, respectively. The A_1 odd-symmetry mode primarily contributes to the ferroelectric polarization in *o-III* phase.

Although all four mode symmetries A_1, A_2, B_1, and B_2 are Raman active, the experimental detection of these modes in the back-scattering geometry is highly sensitive to the orientation of the sample surface with respect to crystal lattice due to the Raman selection rules (see Table S1, Supporting Information). For instance, the B_2 modes can be observed only when the sample surface is parallel to the $\boldsymbol{P}$ [Fig. S3a, Supporting Information], whereas the A_2

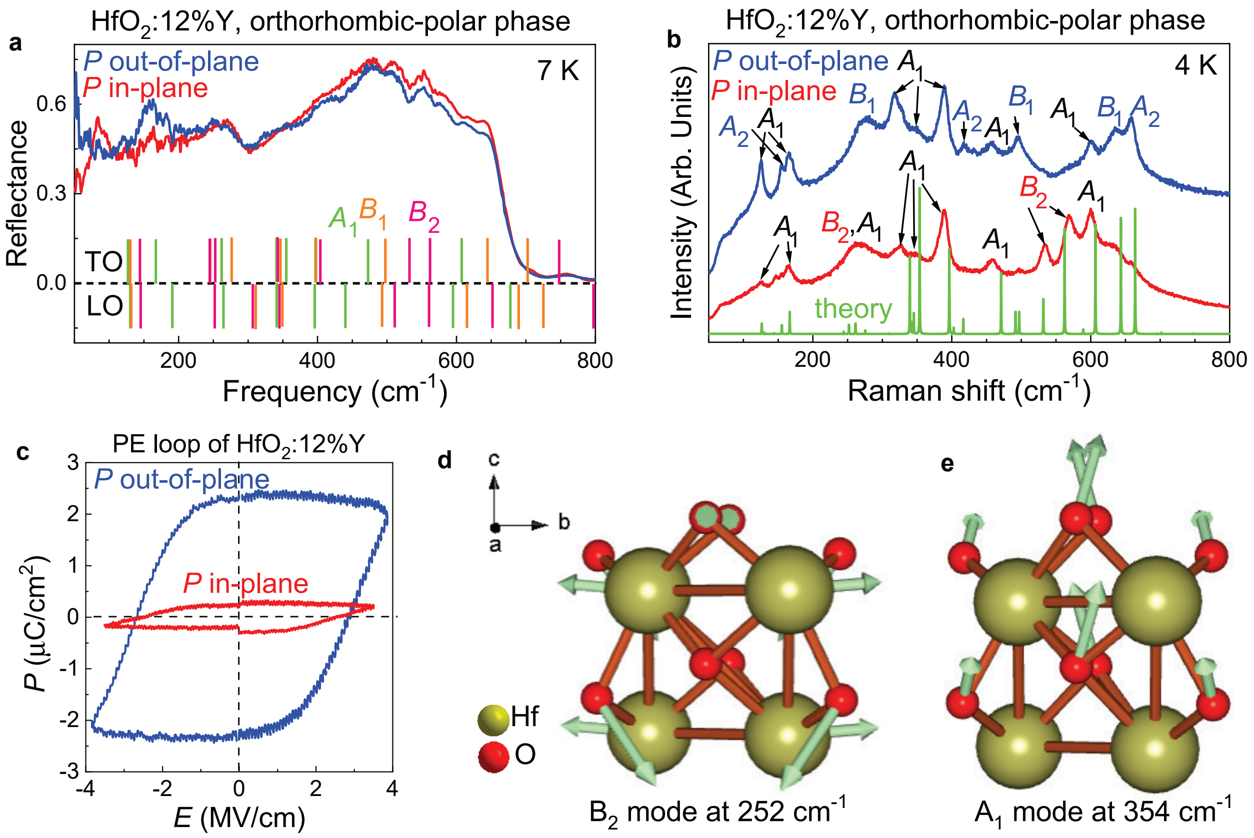

Figure 3. **a,** Infrared reflectance spectra of HfO_2:12% Y for in- and out-of-plane ferroelectric polarization samples measured at 7 K, compared with the theoretically calculated infrared TO and LO peak positions in the pure *o-III* phase. **b,** Raman spectra of HfO_2:12% for the in- and out-of-plane polarization samples measured at 4 K, compared with the theoretically calculated Raman spectrum of the pure *o-III* phase. The measurement geometries are summarized in Table 1 and Fig. S3 of the Supporting Information. **c,** Electric polarization hysteresis loops of the HfO_2:12%Y. Red and blue color indicate polarization along the out-of- and in-plane direction, respectively. **d,e** Calculated phonon displacement patterns for the Hf-Hf breathing mode at 252 cm^{-1}, and the signature polar mode of *o-III* phase at 354 cm^{-1} (see animations in the Supporting Information).

modes can be observed only when the sample surface is perpendicular to the $\boldsymbol{P}$ [Fig. S3b, Supporting Information]. In order to experimentally detect all the Raman-active phonons of the *o-III* phase, we prepared two samples having two different crystallographic surface-cutting directions. Specifically, the surface-normal ($\hat{n}$) orientations are: (i) $\hat{n} \parallel \vec{a}$, $\boldsymbol{P}$-in-plane and (ii) $\hat{n} \perp \vec{a}$, $\boldsymbol{P}$-out-of-plane. The exact measurement geometries are discussed in Fig. S3 of the Supporting Information. Due to the similar lattice parameters, the $\vec{b}$ and $\vec{c}$ axes are finely twinned at the nanoscale in the polar HfO_2:12% Y crystal, which means that the $\vec{b}$ and $\vec{c}$ axes are barely distinguishable in the macroscopic sample.

Figure 3c displays the electric polarization of the two HfO_2:12%Y crystals measured with out-of-plane electric fields. The samples with in- and out-of-surface plane spontaneous ferroelectric polarization are clearly identified in this measurement. Both samples have coercivities with similar amplitudes (approximately 3 MV/cm). The crystal cut to host out-of-surface plane polarization displays a larger measurable remnant polarization (on the order of 2.5 μC/cm^2) compared with the crystal cut to host an in-surface plane polarization, since the applied out-of-plane electric field is only supposed to switch the out-of-plane component of the sample polarization. It is therefore straightforward to distinguish these samples.

Figure 3a,b displays the infrared reflectance and Raman scattering response of the samples with both in- and out-of-surface plane polarizations. Since the infrared response is scalar in nature, the reflectance spectra of both samples are nearly the same; the features observed in the reflectance spectra also nicely match with the calculated frequencies of the infrared-active phonons for the pure hafnia. Similar to HfO_2:20%Y, the weak metallic background partially screens some of the phonon features in the infrared reflectance spectra. The Raman scattering spectra reveal cleaner phonon behavior. The Raman peak positions are well resolved and are easy to track [Fig. 3b].

The crystals with the in- and out-of-surface plane ferroelectric polarization display an overall similar Raman response but with some noticeable differences. The relative intensities of some of the Raman-active phonon modes are slightly different due to the anisotropic character of the polarizability tensor. Another notable difference is that the A_2 and B_1 modes are detected only in the Raman spectrum of the $\boldsymbol{P}$ out-of-surface plane sample, whereas the B_2 modes are observed only in the Raman spectrum of the $\boldsymbol{P}$ in-surface plane sample. This occurs due to the different Raman selection rules for different samples. It is worth mentioning that the B_1 symmetry modes become Raman active in the $\boldsymbol{P}$ out-of-surface plane sample only because the $\vec{b}$ and $\vec{c}$ axes are mixed due to twinning. Observation of the B_2, A_2 and B_1 modes in our Raman measurements is completely consistent with our theoretical predictions summarized in Table S1 of the Supporting Information. Furthermore, our low temperature spectroscopic measurements reveal a weak temperature dependence of both the infrared reflectance and Raman scattering response in this system [Fig. S2, Supporting Information].

Below we highlight two peculiar phonon modes in the *o-III* phase. The first is a Hf-Hf breathing mode of B_2 symmetry near 252 cm^{-1}. Interestingly, the displacement pattern of this Hf-Hf dimer breathing mode, shown in Fig. 3d, has striking similarities to the pantographic Cu-Cu dimer vibration in $SrCu_2(BO_3)_2$, which dramatically modifies the superexchange interaction by modulating the Cu-O-Cu bond angle.[52] Of course, we do not expect the Hf-Hf dimer vibration to significantly affect the properties since hafnia is nonmagnetic. Moreover, a similar Hf-Hf dimer breathing mode is also observed in the experimental spectra of the orthorhombic antipolar and monoclinic phases at nearby frequencies, which implies that it is a fundamental lattice vibrational mode in the low energy phases of hafnia. Second, we identify a signature polar phonon mode of A_1 symmetry near 350 cm^{-1}. We call it a signature mode of the *o-III* phase because there is no Raman peak in all other studies phases of hafnia near the same frequency. The calculated displacement pattern of this A_1 mode, shown in Fig. 3e, reveals that this is the primary polar mode of the *o-III* phase involving polar displacements of oxygen atoms along the $\vec{c}$ lattice vector.[12,21,23] This mode is the closest analogue to the Γ_{15}^{z} polar mode that is responsible for generating scale-free ferroelectricity in hafnia and has been referred as the “flat-phonon band” in literature[12] due to its minuscule dispersion in the momentum space. We observe this mode in the HfO_2:12%Y samples, in both in- and out-of-plane measurement configurations. However, the intensity of this peak is maximized in the sample with the out-of-plane polarization due to its relatively large polarizibility matrix element for the *ac*-plane response. This mode broadens with increasing temperature [Fig. S2, Supporting Information], consistent with the Boltzmann sigmoid model that describes the temperature dependence of phonons.[53,54]

Fingerprinting the different phases of hafnia

Figure 4 summarizes the predicted vibrational properties of the known phases of hafnia. Comparison of the calculated peak positions and relative intensities reveals a number of distinguishing characteristics - more than enough to (i) differentiate two phases from each other or (ii) identify an unknown phase from a spectroscopic measurement. As shown in Fig.

S4 of the Supporting Information, these spectral fingerprints can also be used to identify mixed phases. A detailed summary of the distinguishing features is given in Table S2.

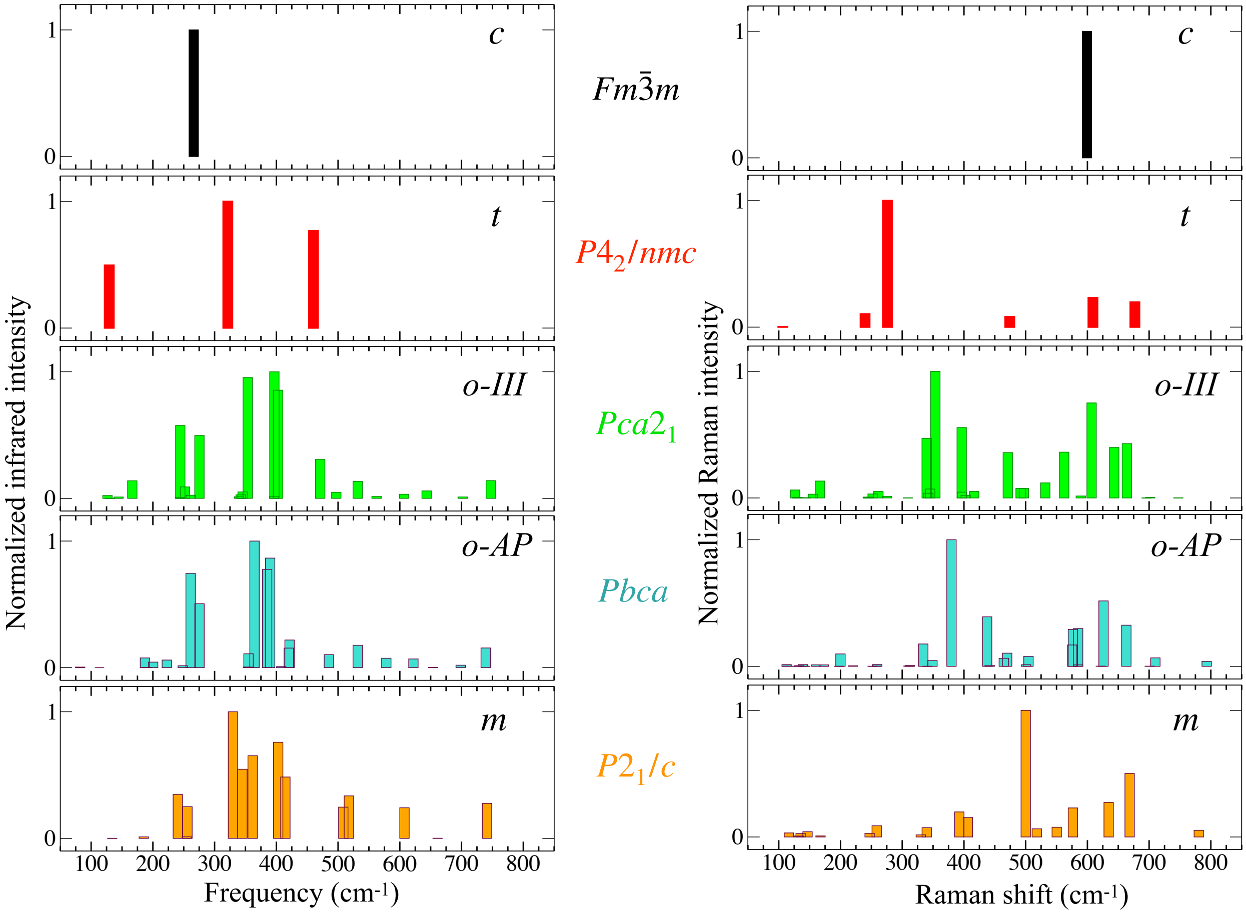

Figure 4. Summary of the calculated (DFT-PBEsol) infrared and Raman responses for the five studied phases of pure hafnia, *i.e.*, cubic (c), tetragonal (t), orthorhombic polar (o-*III*), orthorhombic antipolar (o-*AP*), and monoclinic (m). Only TO infrared modes are provided in the calculated infrared spectra for clarity (see the Supporting Information for details regarding the LO modes).

The cubic phase is the easiest to identify. It has only two signature modes: T_{1u} (infrared active) and T_{2g} (Raman active). The ground state monoclinic phase is also straightforward to identify, although the number of phonons is dramatically increased due to lower crystalline symmetry. Distinguishing features in the infrared response include the B_u symmetry modes at 330 and 518 cm^{-1} as well as A_u symmetry modes at 508 and 607 cm^{-1}. Unique structures in the Raman scattering response include an A_g symmetry peak at 500 cm^{-1} and B_g symmetry modes at 518 and 780 cm^{-1}. The spectrum of monoclinic HfO_2 is well-documented in the literature.[22,40,41]

Analysis is more challenging for the orthorhombic polar and antipolar phases of hafnia due to the complexity of their predicted spectral patterns. We can, however, still pinpoint several unique signatures by closely examining the calculated phonon frequencies and the relative infrared and Raman intensities in Fig. 4. In the infrared response, the A_1 modes at 167 and 471 cm^{-1} and the B_1 modes at 497 and 643 cm^{-1} can be used to identify the *o-III* phase of hafnia. Likewise, the B_{3u} cluster near 200 cm^{-1}, the B_{2u} modes at 385 cm^{-1}, and the B_{1u} phonons at 390, 485, and 622 cm^{-1} establish the *o-AP* phase of hafnia. In the Raman scattering response, the A_1 modes at 354, 396 and 471 cm^{-1} and the B_2 modes at 532 and 562 cm^{-1} can be used as a reference to characterize the *o-III* phase. Note that the detection of the Raman-active modes in the *o-III* phase is dependent on the Raman measurement geometry and different crystallographic surface-cutting directions with respect to the spontaneous ferroelectric polarization directions. For the *o-AP* phase, the Raman-active A_g symmetry modes at 200, 380, and 438 cm^{-1} and the B_{2g} mode at 710 cm^{-1} are the signature structures.

Finally, we discuss the vibrational properties of the tetragonal phase of hafnia. Although not yet grown in a single crystal form, this phase will be readily identifiable once it becomes available. Unique signatures are predicted to include a strong infrared-active A_{2u} mode at 321 cm^{-1} and an intense Raman-active A_{1g} mode at 276 cm^{-1}. No infrared or Raman peaks are predicted to exist at these frequencies in any other phases of hafnia. The infrared-active E_u mode at 129 cm^{-1} and the Raman-active E_g mode at 677 cm^{-1} are additional characteristics of the tetragonal phase.

Charge-structure-function relationships in the different phases of hafnia

In order to extend our understanding of structure-property relationships in this family of materials, we analyzed the calculated Born effective charges ($\mathbf{Z}^*$) for each phase of HfO_2. These results are summarized in Table S3 of the Supporting Information and are in good agreement with the previous data reported on the c, t, and m phases.[40] We find that the $\mathbf{Z}^*$ tensor varies dramatically with the different phases of hafnia. In addition to the observed differences in anisotropy in the low-symmetry phases, we note that $\mathbf{Z}^*$ of Hf can acquire a value as large as $+5.56\,\mathrm{e}^-$ in the cubic phase to relatively smaller values nearing $+5\,\mathrm{e}^-$ in the lower symmetry phases of hafnia (lowest $Z^*_{Hf} = +4.83\,\mathrm{e}^-$ in the m phase). In each case, the Z^*_{Hf} is larger than the nominal valence charge of the Hf atoms ($+4\,\mathrm{e}^-$). Such an anomalously large Z^*_{Hf}, exceeding the Madelung limit, indicates a strong dynamic charge transfer from oxygen to hafnium atoms along the Hf-O bond. It further implies the mixed ionic-covalent nature of the Hf-O bonds in hafnia. Similar behavior has been observed in 1T-HfS_2 ($Z^*_{Hf} = +5.3\,\mathrm{e}^-$).[45]

SUMMARY AND OUTLOOK

Looking ahead, many of the metastable phases of HfO_2 discussed in this work will find application in emerging chip technologies. Naturally, properties like thermal conductivity and heat capacity are key to effective heat management. Useful microscopic models of dissipation in these high κ dielectrics will require information about the fundamental excitations of the lattice. That first principles methods can so accurately predict phonon eigenvectors and intensities bodes well for these modeling efforts. At the same time, this work opens the door to phononic engineering of hafnia-containing device architectures where strategies to block damaging lattice effects can be tested and evaluated in advance of any measurement, significantly extending the complexity of chip modeling efforts.

METHODS

Crystal growth and sample preparation: HfO_2:x%Y crystals were grown utilizing laser-diode-heated floating zone techniques.[13] The optimal growth conditions were 95% laser power (approximately 3000 K), atmospheric air flow of 0.1 L min^{-1}, and counter-rotation of the feed and seed rods at 3 and 20 rpm, respectively. Rapid cooling is one of the key factors to stabilize meta-stable phases. Therefore, growth rate of 20 mm/h or a subsequent laser quench process, i.e. quickly scanning the crystal by 65% power laser-heated zone, were performed to reach very high cooling rates. The crystal rods were oriented by Laue back-reflection x-ray methods and cut into ab/ac and bc plates, with typical size $\approx 2 \times 2$ mm^2. All samples were polished to reveal shiny, flat surfaces suitable for spectroscopy. A summary of the growth and processing conditions of our various samples is given in Table 1.

Table 1. **Summary of HfO_2 single crystals with different Y substitutions.**

HfO_2: x%Y crystals	20%	12%, $\vec{P}$ in-plane	12%, $\vec{P}$ out-of-plane	11%	8%	0%
Structure and phase	Cubic non-polar	Orthorhombic polar	Orthorhombic polar	Orthorhombic antipolar	Mixing of orthorhombic antipolar and monoclinic	Monoclinic non-polar
Surface cutting	Random	$\vec{P}$ in-plane (bc)	$\vec{P}$ out-of-plane (ab/ac)	Pseudo-cubic	Pseudo-cubic	Random
Polarization direction	None	bc-plane	ab- or ac-plane	None	None	None
Measurement geometry	$\vec{k} \perp$ surface	$\vec{k} \parallel a$	$\vec{k} \perp a$	$\vec{k} \perp$ surface	$\vec{k} \perp$ surface	$\vec{k} \perp$ surface
Growth rate	20 mm/h	20 mm/h	20 mm/h	20 mm/h	4 mm/h	4 mm/h
Quench rate	20 mm/h	20 mm/h	20 mm/h	20 mm/h	300 mm/h	–

Infrared and Raman scattering response: We measured the infrared reflectance of a series of Y-substituted HfO_2 single crystals [Table 1] using a series of Fourier transform spectrometers equipped with liquid helium- and nitrogen-cooled detectors. In this work, we focus on the 20 - 850 cm^{-1} frequency range. Raman scattering measurements were performed in the back scattering geometry with normal incident and unpolarized light using a LabRAM HR Evolution spectrometer. Different excitations lasers (λ_{excit} = 476, 532, and 785 nm; $\leq$ 3.2 mW) were employed as appropriate. Each scan was integrated for 60 s and averaged 5 times. Temperature control was achieved with an open-flow cryostat (350 - 4 K).

Symmetry analysis and lattice dynamics calculations: First principles density functional theory (DFT) calculations were performed using the projector augmented wave method as implemented in the Vienna Ab initio Simulation Package (VASP).[55–57] The exchange-correlation functional was computed using the generalized-gradient approximation as parameterized by Perdew-Burke-Ernzerhof for solids (PBEsol).[58] 600 eV was used as the kinetic energy cutoff for plane waves. The energy convergence criterion for self-consistent DFT calculations was set at 10^{-7} eV and force convergence criterion for relaxation of atomic coordinates was set at 10^{-3} eV/Å. The reciprocal space of the cubic (c), tetragonal (t), orthorhombic polar (o-III), orthorhombic antipolar (o-AP), and monoclinic (m) phases was sampled using a Monkhorst-pack k-mesh[59] of size 8×8×8, 12×12×8, 8×8×8, 8×8×4, and 8×8×6, respectively. The phonon dispersions of the c, t, o-III, o-AP, and m phases were calculated using supercells of size 4×4×4, 4×4×2, 2×2×2, 2×1×2, and 2×2×2, respectively. The non-analytical term correction was employed using the Gonze scheme[60,61] as implemented in the PHONOPY package.[62] A commensurate k-grid was used for phonon calculations. The zone-center phonon eigenvectors were used to compute the theoretical infrared and Raman spectra using the methods described in Ref.[63] An appropriate averaging of the Raman-activity tensor was done to simulate the Raman spectrum of each studies phases of hafnia. The Bilbao Crystallographic Server,[64] PHONON website,[65] and PHONOPY package[62] were utilized to determine the Raman selection rules and symmetry of the phonon modes.

ACKNOWLEDGEMENTS

S.F., K.P., and J.L.M. appreciate support from the National Science Foundation (DMR-2129904 and DMR-1629079) and the Materials Research Fund at the University of Tennessee. X.X. and S.W.C. were supported by the center for Quantum Materials Synthesis (cQMS), funded by the Gordon and Betty Moore Foundation's EPiQS initiative through grant GBMF6402, and by Rutgers University. S.S., Y.Q., and K.M.R. acknowledge funding from Office of Naval Research (ONR) grant N00014-21-1-2107. D.V. acknowledges support from National Science Foundation grant DMR-1954856. First-principles calculations were performed using the computational resources provided by the Rutgers University Parallel Computing clusters.

CONTRIBUTIONS

This project was conceived by J.L.M. and S.W.C. The single crystals were grown and polarization loop measured by X.X. with advice from S.W.C. The spectroscopic work was performed by S.F. and K.P. with advice from J.L.M. The first principles DFT calculations were carried out by S.S. with advice from D.V. and K.M.R. Data analysis was completed by S.F., S.S., K.P., Y.Q., D.V., K.M.R., and J.L.M. All authors discussed the findings. The manuscript was written by S.F., S.S., X.X., K.P., K.M.R., and J.L.M. All authors read and commented on the manuscript.

COMPETING INTERESTS

The authors declare no competing interests.

CORRESPONDING AUTHORS

Direct correspondence to Janice L. Musfeldt (musfeldt@utk.edu) and Karin M. Rabe (rabe@physics.rutgers.edu).

DATA AVAILABILITY

Relevant data are available upon request from the corresponding authors.

[1] Wilk, G. D., Wallace, R. M. & Anthony, J. M. High-κ gate dielectrics: current status and materials properties considerations. *Journal of Applied Physics* **89**, 5243–5275 (2001). URL `https://doi.org/10.1063/1.1361065`.

[2] Hoffmann, M., Slesazeck, S., Schroeder, U. & Mikolajick, T. What's next for negative capacitance electronics? *Nature Electronics* **3**, 504–506 (2020). URL `https://doi.org/10.1038/s41928-020-00474-9`.

[3] Clima, S. *et al.* Identification of the ferroelectric switching process and dopant-dependent switching properties in orthorhombic HfO_2: A first principles insight. *Applied Physics Letters* **104**, 092906 (2014). URL `https://doi.org/10.1063/1.4867975`.

[4] Böscke, T. S., Müller, J., Bräuhaus, D., Schröder, U. & Böttger, U. Ferroelectricity in hafnium oxide thin films. *Applied Physics Letters* **99**, 102903 (2011). URL `https://doi.org/10.1063/1.3634052`.

[5] Park, M. H., Lee, Y. H., Mikolajick, T., Schroeder, U. & Hwang, C. S. Review and perspective on ferroelectric HfO_2-based thin films for memory applications. *MRS Communications* **8**, 795–808 (2018). URL `https://doi.org/10.1557/mrc.2018.175`.

[6] Zhou, D. *et al.* Electric field and temperature scaling of polarization reversal in silicon doped hafnium oxide ferroelectric thin films. *Acta Materialia* **99**, 240–246 (2015). URL `https://www.sciencedirect.com/science/article/pii/S1359645415005066`.

[7] Alessandri, C., Pandey, P., Abusleme, A. & Seabaugh, A. Switching dynamics of ferroelectric Zr-doped HfO_2. *IEEE Electron Device Letters* **39**, 1780–1783 (2018). URL `https://ieeexplore.ieee.org/document/8472268/`.

[8] Choe, D.-H. *et al.* Unexpectedly low barrier of ferroelectric switching in HfO_2 via topological domain walls. *Materials Today* (2021). URL `https://www.sciencedirect.com/science/article/pii/S136970212100256X`.

[9] Wei, Y. *et al.* A rhombohedral ferroelectric phase in epitaxially strained $Hf_{0.5}Zr_{0.5}O_2$ thin films. *Nature Materials* **17**, 1095–1100 (2018). URL `https://doi.org/10.1038/s41563-018-0196-0`.

[10] Cheema, S. S. *et al.* Enhanced ferroelectricity in ultrathin films grown directly on silicon. *Nature* **580**, 478–482 (2020). URL `https://doi.org/10.1038/s41586-020-2208-x`.

[11] Park, M. H., Lee, Y. H., Mikolajick, T., Schroeder, U. & Hwang, C. S. Thermodynamic and kinetic origins of ferroelectricity in fluorite structure oxides. *Advanced Electronic Materials* **5**, 1800522 (2019). URL `https://onlinelibrary.wiley.com/doi/abs/10.1002/aelm.201800522`.

[12] Lee, H.-J. *et al.* Scale-free ferroelectricity induced by flat phonon bands in HfO_2. *Science* **369**, 1343–1347 (2020). URL `https://science.sciencemag.org/content/369/6509/1343`.

[13] Xu, X. *et al.* Kinetically stabilized ferroelectricity in bulk single-crystalline HfO_2:Y. *Nature Materials* **20,**, 826–832 (2021). URL `https://doi.org/10.1038/s41563-020-00897-x`.

[14] Mikolajick, T. & Schroeder, U. Ferroelectricity in bulk hafnia. *Nature Materials* **20**, 718–719 (2021). URL `https://doi.org/10.1038/s41563-020-00914-z`.

[15] Jiang, P. *et al.* Wake-up effect in HfO_2-based ferroelectric films. *Advanced Electronic Materials* **7**, 2000728 (2021). URL `https://onlinelibrary.wiley.com/doi/abs/10.1002/aelm.202000728`.

[16] Mandal, G. & Das, P. The pressure induced structural phase transition of HfO_2. *AIP Conference Proceedings* **1832**, 030014 (2017). URL `https://aip.scitation.org/doi/abs/10.1063/1.4980193`.

[17] Huan, T. D., Sharma, V., Rossetti, G. A. & Ramprasad, R. Pathways towards ferroelectricity in hafnia. *Phys. Rev. B* **90**, 064111 (2014). URL `https://link.aps.org/doi/10.1103/PhysRevB.90.064111`.

[18] Breyer, E. T., Mulaosmanovic, H., Mikolajick, T. & Slesazeck, S. Perspective on ferroelectric, hafnium oxide based transistors for digital beyond von-Neumann computing. *Appl. Phys. Lett.* **118**, 050501 (2021). URL `https://doi.org/10.1063/5.0035281`.

[19] Park, M. H. *et al.* Ferroelectricity and antiferroelectricity of doped thin HfO_2-based films. *Advanced Materials* **27**, 1811–1831 (2015). URL `https://onlinelibrary.wiley.com/doi/abs/10.1002/adma.201404531`.

[20] Qi, Y. *et al.* Stabilization of competing ferroelectric phases of HfO_2 under epitaxial strain. *Phys. Rev. Lett.* **125**, 257603 (2020). URL `https://link.aps.org/doi/10.1103/PhysRevLett.125.257603`.

[21] Qi, Y. & Rabe, K. M. Phase competition in HfO_2 with applied electric field from first principles. *Phys. Rev. B* **102**, 214108 (2020). URL `https://link.aps.org/doi/10.1103/PhysRevB.102.214108`.

[22] Cojocaru, B. *et al.* Phase control in hafnia: new synthesis approach and convergence of average and local structure properties. *ACS Omega* **4**, 8881–8891 (2019). URL `https://doi.org/10.1021/acsomega.9b00580`.

[23] Delodovici, F., Barone, P. & Picozzi, S. Trilinear-coupling-driven ferroelectricity in HfO_2. *Physical Review Materials* **5** (2021). URL `http://dx.doi.org/10.1103/PhysRevMaterials.5.064405`.

[24] Wang, J., Li, H. P. & Stevens, R. Hafnia and hafnia-toughened ceramics. *Journal of Materials Science* **27**, 5397–5430 (1992). URL `https://doi.org/10.1007/BF00541601`.

[25] Arashi, H. Pressure-induced phase transformation of HfO_2. *Journal of the American Ceramic Society* **75**, 844–847 (1992). URL `https://ceramics.onlinelibrary.wiley.com/doi/abs/10.1111/j.1151-2916.1992.tb04149.x`.

[26] Jayaraman, A., Wang, S. Y., Sharma, S. K. & Ming, L. C. Pressure-induced phase transformations in HfO_2 to 50 GPa studied by Raman spectroscopy. *Phys. Rev. B* **48**, 9205–9211 (1993). URL `https://link.aps.org/doi/10.1103/PhysRevB.48.9205`.

[27] Low, J. J., Paulson, N. H., D'Mello, M. & Stan, M. Thermodynamics of monoclinic and tetragonal hafnium dioxide (HfO_2) at ambient pressure. *Calphad* **72**, 102210 (2021). URL `https://www.sciencedirect.com/science/article/pii/S0364591620304739`.

[28] Reyes-Lillo, S. E., Garrity, K. F. & Rabe, K. M. Antiferroelectricity in thin-film ZrO_2 from first principles. *Phys. Rev. B* **90**, 140103 (2014). URL `https://link.aps.org/doi/10.1103/PhysRevB.90.140103`.

[29] Shimizu, T. *et al.* The demonstration of significant ferroelectricity in epitaxial Y-doped HfO_2 film. *Scientific Reports* **6**, 32931 (2016). URL `https://doi.org/10.1038/srep32931`.

[30] Zhang, Z. *et al.* Epitaxial ferroelectric $Hf_{0.5}Zr_{0.5}O_2$ with metallic pyrochlore oxide electrodes. *Advanced Materials* **33**, 2006089 (2021). URL `https://onlinelibrary.wiley.com/doi/abs/10.1002/adma.202006089`.

[31] Wang, C., Qiao, H. & Kim, Y. Perspective on the switching behavior of HfO_2-based ferroelectrics. *Journal of Applied Physics* **129**, 010902 (2021). URL `https://doi.org/10.1063/5.0035652`.

[32] Rushchanskii, K. Z., Blügel, S. & Ležaić, M. Ordering of oxygen vacancies and related ferroelectric properties in $HfO_{2-\delta}$. *Phys. Rev. Lett.* **127**, 087602 (2021). URL `https://link.aps.org/doi/10.1103/PhysRevLett.127.087602`.

[33] Park, M. H. *et al.* A comprehensive study on the structural evolution of HfO_2 thin films doped with various dopants. *J. Mater. Chem. C* **5**, 4677–4690 (2017). URL `http://dx.doi.org/10.1039/C7TC01200D`.

[34] Fina, I. & Sánchez, F. Epitaxial ferroelectric HfO_2 films: Growth, properties, and devices. *ACS Applied Electronic Materials* **3**, 1530–1549 (2021). URL `https://doi.org/10.1021/acsaelm.1c00110`.

[35] Nukala, P. *et al.* Reversible oxygen migration and phase transitions in hafnia-based ferroelectric devices. *Science* **372**, 630–635 (2021). URL `https://science.sciencemag.org/content/early/2021/04/14/science.abf3789`.

[36] Anastassakis, E., Papanicolaou, B. & Asher, I. Lattice dynamics and light scattering in hafnia and zirconia. *Journal of Physics and Chemistry of Solids* **36**, 667–676 (1975). URL `https://www.sciencedirect.com/science/article/pii/0022369775900852`.

[37] Kourouklis, G. A. & Liarokapis, E. Pressure and temperature dependence of the Raman spectra of zirconia and hafnia. *Journal of the American Ceramic Society* **74**, 520–523 (1991). URL `https://ceramics.onlinelibrary.wiley.com/doi/abs/10.1111/j.1151-2916.1991.tb04054.x`.

[38] Carlone, C. Raman spectrum of zirconia-hafnia mixed crystals. *Phys. Rev. B* **45**, 2079–2084 (1992). URL `https://link.aps.org/doi/10.1103/PhysRevB.45.2079`.

[39] Kim, B.-K. & Hamaguchi, H.-o. Raman spectrum of 18o-labelled hafnia. *Materials Research Bulletin* **32**, 1367–1370 (1997). URL `https://www.sciencedirect.com/science/article/pii/S0025540897001141`.

[40] Zhao, X. & Vanderbilt, D. First-principles study of structural, vibrational, and lattice dielectric properties of hafnium oxide. *Phys. Rev. B* **65**, 233106 (2002). URL `https://link.aps.org/doi/10.1103/PhysRevB.65.233106`.

[41] Belo, G. *et al.* Phase transition in sputtered HfO_2 thin films: A qualitative Raman study. *Applied Surface Science* **261**, 727–729 (2012). URL `https://www.sciencedirect.com/science/article/pii/S0169433212014663`.

[42] Kumar, H. P. *et al.* Optical properties of nanocrystalline HfO_2 synthesized by an auto-igniting combustion synthesis. *Journal of Asian Ceramic Societies* **3**, 64–69 (2015). URL `https://doi.org/10.1016/j.jascer.2014.10.009`.

[43] Singhal, R. *et al.* Synthesis, structural, Raman scattering and magnetic properties of Fe -doped HfO_2 nanoparticles. *Materials Research Express* **6**, 096117 (2019). URL `https://doi.org/10.1088/2053-1591/ab0927`.

[44] Acevedo, D. *et al.* Raman spectra of high-k dielectric layers investigated with micro-Raman spectroscopy comparison with silicon dioxide. *The Scientific World Journal* **2013**, 208081 (2013). URL `https://doi.org/10.1155/2013/208081`.

[45] Neal, S. N., Li, S., Birol, T. & Musfeldt, J. L. Chemical bonding and Born charge in 1T-HfS_2. *npj 2D Materials and Applications* **5**, 45 (2021). URL `https://doi.org/10.1038/s41699-021-00226-z`.

[46] Liu, D. W., Perry, C. H. & Ingel, R. P. Infrared spectra in nonstoichiometric yttria-stabilized zirconia mixed crystals at elevated temperatures. *Journal of Applied Physics* **64**, 1413–1417 (1988). URL `https://doi.org/10.1063/1.341839`.

[47] Peng, W. *et al.* Oxygen vacancy-induced topological nanodomains in ultrathin ferroelectric films. *npj Quantum Mater.* **6**, 48 (2021). URL `http://www.nature.com/articles/s41535-021-00349-y`.

[48] Frederick, H. M. Experimental determination of emissivity and resistivity of yttria stabilized zirconia at high temperatures. *Master's Thesis, University of Tennessee.* (2008). URL `https://trace.tennessee.edu/utk_gradthes/377/`.

[49] Yokosuk, M. & *et al*. Unraveling the competition between structure, metalicity, and magnetism in Nb-substituted $EuTiO_3$. *In preparation* (2021).

[50] Gervais, F. Optical conductivity of oxides. *Materials Science and Engineering: R: Reports* **39**, 29–92 (2002). URL `https://www.sciencedirect.com/science/article/pii/S0927796X02000736`.

[51] Petit, N., Soret, J.-C. & Gervais, F. Analysis of concentration dependence of optical conductivity of $BaPb_{1-x}Bi_xO_3$ revisited. *Solid State Communications* **110**, 621–626 (1999). URL `https://www.sciencedirect.com/science/article/pii/S0038109899001106`.

[52] Radtke, G., Saúl, A., Dabkowska, H. A., Salamon, M. B. & Jaime, M. Magnetic nanopantograph in the $SrCu_2(BO_3)_2$ Shastry–Sutherland lattice. *Proceedings of the National Academy of Sciences* **112**, 1971–1976 (2015). URL `https://www.pnas.org/content/112/7/1971`.

[53] Yokosuk, M. O. *et al.* Tracking the continuous spin-flop transition in Ni_3TeO_6 by infrared spectroscopy. *Phys. Rev. B* **92**, 144305 (2015). URL `https://link.aps.org/doi/10.1103/PhysRevB.92.144305`.

[54] Fan, S. *et al.* Excitations of intercalated metal monolayers in transition metal dichalcogenides. *Nano Letters* **21**, 99–106 (2021). URL `https://doi.org/10.1021/acs.nanolett.0c03292`.

[55] Kresse, G. & Furthmüller, J. Efficient iterative schemes for *ab initio* total-energy calculations using a plane-wave basis set. *Phys. Rev. B* **54**, 11169–11186 (1996). URL `https://link.aps.org/doi/10.1103/PhysRevB.54.11169`.

[56] Kresse, G. & Furthmüller, J. Efficiency of *ab-initio* total energy calculations for metals and semiconductors using a plane-wave basis set. *Computational Materials Science* **6**, 15 – 50 (1996). URL `http://www.sciencedirect.com/science/article/pii/0927025696000080`.

[57] Kresse, G. & Joubert, D. From ultrasoft pseudopotentials to the projector augmented-wave method. *Phys. Rev. B* **59**, 1758–1775 (1999). URL `https://link.aps.org/doi/10.1103/PhysRevB.59.1758`.

[58] Perdew, J. P. *et al.* Restoring the density-gradient expansion for exchange in solids and surfaces. *Phys. Rev. Lett.* **100**, 136406 (2008). URL `https://link.aps.org/doi/10.1103/PhysRevLett.100.136406`.

[59] Monkhorst, H. J. & Pack, J. D. Special points for Brillouin-zone integrations. *Phys. Rev. B* **13**, 5188–5192 (1976). URL `https://link.aps.org/doi/10.1103/PhysRevB.13.5188`.

[60] Gonze, X., Charlier, J.-C., Allan, D. & Teter, M. Interatomic force constants from first principles: The case of α-quartz. *Phys. Rev. B* **50**, 13035–13038 (1994). URL `https://link.aps.org/doi/10.1103/PhysRevB.50.13035`.

[61] Gonze, X. & Lee, C. Dynamical matrices, Born effective charges, dielectric permittivity tensors, and interatomic force constants from density-functional perturbation theory. *Phys. Rev. B* **55**, 10355–10368 (1997). URL `https://link.aps.org/doi/10.1103/PhysRevB.55.10355`.

[62] Togo, A. & Tanaka, I. First principles phonon calculations in materials science. *Scr. Mater.* **108**, 1–5 (2015). URL `https://doi.org/10.1016/j.scriptamat.2015.07.021`.

[63] Skelton, J. M. *et al.* Lattice dynamics of the tin sulphides SnS_2, SnS and Sn_2S_3: vibrational spectra and thermal transport. *Phys. Chem. Chem. Phys.* **19**, 12452–12465 (2017). URL `http://dx.doi.org/10.1039/C7CP01680H`.

[64] Kroumova, E. *et al.* Bilbao crystallographic server : useful databases and tools for phase-transition studies. *Phase Transitions* **76**, 155–170 (2003). URL `https://doi.org/10.1080/0141159031000076110`.

[65] Http://henriquemiranda.github.io/phononwebsite/phonon.html.